



This is a repository copy of *Ni-Co-Mn-Ti-B high performance multiferroic phase transformation material: simultaneous modulation of mechanical properties and successive caloric effects by B doping*.

White Rose Research Online URL for this paper:

<https://eprints.whiterose.ac.uk/202531/>

Version: Accepted Version

Article:

Guan, Z., Bai, J., Zhang, Y. et al. (6 more authors) (2023) Ni-Co-Mn-Ti-B high performance multiferroic phase transformation material: simultaneous modulation of mechanical properties and successive caloric effects by B doping. *Materials Today Physics*, 36. 101183. ISSN 2542-5293

<https://doi.org/10.1016/j.mtphys.2023.101183>

Article available under the terms of the CC-BY-NC-ND licence
(<https://creativecommons.org/licenses/by-nc-nd/4.0/>).

Reuse

This article is distributed under the terms of the Creative Commons Attribution-NonCommercial-NoDerivs (CC BY-NC-ND) licence. This licence only allows you to download this work and share it with others as long as you credit the authors, but you can't change the article in any way or use it commercially. More information and the full terms of the licence here: <https://creativecommons.org/licenses/>

Takedown

If you consider content in White Rose Research Online to be in breach of UK law, please notify us by emailing eprints@whiterose.ac.uk including the URL of the record and the reason for the withdrawal request.



eprints@whiterose.ac.uk
<https://eprints.whiterose.ac.uk/>

Ni-Co-Mn-Ti-B high performance multiferroic phase transformation material: Simultaneous modulation of mechanical properties and successive caloric effects by B doping

Ziqi Guan ^a, Jing Bai ^{a,b,*}, Yu Zhang ^a, Jianglong Gu ^c, Nicola Morley ^d, Yudong Zhang ^e, Claude Esling ^e, Xiang Zhao ^a, Liang Zuo ^{a,**}

^a Key Laboratory for Anisotropy and Texture of Materials, School of Material Science and Engineering, Northeastern University, Shenyang, 110819, China

^b Key Laboratory of Dielectric and Electrolyte Functional Material Hebei Province, School of Resources and Materials, Northeastern University at Qinhuangdao, Qinhuangdao, 066004, PR China

^c State Key Laboratory of Metastable Materials Science and Technology, Yanshan University, Qinhuangdao, 066004, PR China

^d Department of Material Science and Engineering, University of Sheffield, Sheffield, S1 3JD, UK

^e Laboratoire D'Etude des Microstructures et de Mécanique des Matériaux, LEM3, CNRS, UMR 7239, University of Lorraine, 57045, Metz, France

ABSTRACT

Ni-Mn-based multiferroic phase transformation materials are emerging as one of the most promising candidates in the field of solid-state refrigeration. However, the high intrinsic brittleness and the narrow working temperature region of these alloys limit their practical applications. Here, we demonstrate a composition design strategy for B doping in Ni-Co-Mn-Ti alloys, which simultaneously improves mechanical properties and maintains giant successive caloric effects with a broad working region near room temperature. Our results reveal that the original Ti-rich second phase in the Ni-Co-Mn-Ti alloys has little contribution to the mechanical properties, while the grain refinement and grain boundary strengthening mechanisms formed by the doping of B can ensure excellent mechanical properties. Through composition optimization, the $(\text{Ni}_{37}\text{Co}_{13}\text{Mn}_{34}\text{Ti}_{16})_{98.5}\text{B}_{1.5}$ alloy prepared by arc melting can exhibit excellent mechanical properties and functional behavior. The fracture compressive strength and strain can reach up to 1553 MPa and 17.7% at 290 K, respectively. Besides, the maximum magnetic entropy change induced by a 7 T magnetic field is $40.3 \text{ J}\cdot\text{kg}^{-1}\cdot\text{K}^{-1}$, and a large elastocaloric adiabatic temperature change of 18.0 K can be yielded by applying a stress field. A combination of magnetocaloric and elastocaloric effects can achieve a broad working temperature region of over 90 K.

Keywords: Ni-Co-Mn-Ti-B Heusler alloy; Martensitic transformation; Mechanical properties; Magnetocaloric effect; Elastocaloric effect

1. Introduction

The solid-state refrigeration technique has become an imperative technology in contemporary society, because of its energy-efficient and it does not produce greenhouse gases, it is regarded as a promising alternative technique to conventional vapor-compression refrigeration [1-3]. In recent years, the main emerging solid-state refrigeration techniques based on the caloric effects are the magnetocaloric effect (MCE) [4-7], elastocaloric effect (eCE) [8-11], electrocaloric effect (ECE) [12], and barocaloric effect (BCE) [13-15] refrigeration. These caloric effects originate from the latent heat generated during phase transition of solid-state refrigeration materials induced by different driving fields. Currently, most solid-state refrigeration materials exhibit only a single-caloric effect with a narrow working temperature region. In order to broaden the working region of caloric effect materials, researchers have focused on multiferroic materials. The expectation is to combine the different caloric effects of the materials to achieve the combined caloric effects to widen the working temperature region. Ni-Mn-based Heusler-type shape memory alloys can combine ferroelastic and ferromagnetic order, and display intriguing multicaloric effects (eCE, MCE, and BCE). This offers an unique possibility for developing new solid-state refrigeration materials [16-18].

At present, researchers have conducted extensive studies on various Ni-Mn-based Heusler alloys. Hu et al. [19] simultaneously found eCE and MCE in directionally solidified Ni_{49.5}Mn₂₈Ga_{22.5} alloy and doubled the working temperature region by combining eCE and MCE. Qu et al. [20] have reported that the Ni₄₃Co₆Mn₄₀Sn₁₁ alloy achieved a large elastocaloric adiabatic temperature change (ΔT_{ad}) of 7.1 K under a stress of 550 MPa. In addition, the reversible magnetic entropy change ($\otimes S_m$) of this alloy under magnetic field changes of 5 T is 19.3 J·kg⁻¹·K⁻¹. Li et al. [21] demonstrated that a giant ΔT_{ad} of up to 19.7 K is obtained in directionally solidified Ni₅₀Mn₃₅In₁₅ alloy on removing a stress of 350 MPa, and the maximum $\otimes S_m$ can reach 22.9 J·kg⁻¹·K⁻¹ under the field changes of 5 T. The above studies suggest that both MCE and eCE can be observed in Ni-Mn-based Heusler alloys, and a broad working temperature can be achieved by combining these two types of caloric effects. Nevertheless, the inherent brittleness of these alloys jeopardizes their functional behavior for practical applications, and their mechanical properties remain poor even after special processes such as directional solidification or single crystal growth [8, 21].

Recently, Ni-Mn-Ti-based all-d-metal alloys have been widely studied as a novel Heusler alloy. This alloy system has both excellent mechanical properties and large eCE during stress-induced phase transformation [22-24]. However, the Ni-Mn-Ti alloy doesn't possess significant MCE as the other conventional NiMn-based alloys since both the austenite and martensite exhibit weak magnetism. To introduce the MCE in Ni-Mn-Ti alloy, some researchers have tried to dope with the Co element [25-27]. Although Co doping can establish the magnetostructural coupling in the Ni-Mn-Ti alloys, the

doping of Co considerably weakens the eCE and mechanical properties of alloys [29]. In order to improve the mechanical properties of Ni-Co-Mn-Ti alloys for practical applications, some special processes are still required. This will considerably increase the cost and process steps for alloy preparation. Therefore, the preparation of low-cost Ni-Co-Mn-Ti alloys with combined caloric effects and excellent mechanical properties is a great challenge.

In the present work, we have greatly improved the mechanical properties of the Ni-Co-Mn-Ti alloys by doping with the B element while maintaining a giant MCE. Besides, the doping of B can also tune the martensitic transformation (MT) temperature and Curie temperature (T_C), enabling the combination of MCE and eCE for the alloy to achieve a successive caloric effect. Especially, the $(\text{Ni}_{37}\text{Co}_{13}\text{Mn}_{34}\text{Ti}_{16})_{98.5}\text{B}_{1.5}$ alloy simultaneously possesses excellent mechanical properties and a large combined caloric effect with a wide working temperature region of over 90 K.

2. Experimental methods

To study the effect of boron doping on the mechanical properties and caloric effects of the $(\text{Ni}_{37}\text{Co}_{13}\text{Mn}_{34}\text{Ti}_{16})_{100-x}\text{B}_x$ ($x = 0\sim 3$) alloys, polycrystalline ingots were synthesized by arc melting under the high-purity argon atmosphere (for the convenience of description, these alloys were denoted as $\text{Co}_{13}\text{Ti}_{16}$, $(\text{Co}_{13}\text{Ti}_{16})\text{B}_{0.2}$, $(\text{Co}_{13}\text{Ti}_{16})\text{B}_{0.4}$, $(\text{Co}_{13}\text{Ti}_{16})\text{B}_{0.6}$, $(\text{Co}_{13}\text{Ti}_{16})\text{B}_{0.8}$, $(\text{Co}_{13}\text{Ti}_{16})\text{B}_{1.2}$, $(\text{Co}_{13}\text{Ti}_{16})\text{B}_{1.5}$, $(\text{Co}_{13}\text{Ti}_{16})\text{B}_{2.0}$, and $(\text{Co}_{13}\text{Ti}_{16})\text{B}_{3.0}$, respectively). For homogeneity, these ingots were annealed at 1223 K for 2 days followed by quenching into cold water. The crystal structure of alloys was conducted on powder X-ray diffraction (XRD) employing Cu-K α radiation. The microstructure of the specimens was characterized by a scanning electron microscope (SEM) equipped with an energy dispersive spectrometer (EDS). Transmission electron microscopy (TEM) was performed to characterize the crystalline structure and microstructure of the samples. Differential scanning calorimetry (DSC) was used to measure the characteristic temperatures of the reversible martensitic transformation (M_s , M_f , A_s , and A_f). The measurements of the magnetic properties were carried out using a Quantum interference device (MPMS-3). Samples of $3 \times 4 \times 6 \text{ mm}^3$ were cut in the center of the polycrystalline ingots for the compression tests. The ΔT_{ad} values of loading and unloading the external stress were directly monitored using a K-type thermocouple at RT.

3. Results and discussion

3.1. Martensitic transformation and crystal structure

To investigate the effect of doping with boron on MT and crystal structure in the $(\text{Ni}_{37}\text{Co}_{13}\text{Mn}_{34}\text{Ti}_{16})_{100-x}\text{B}_x$ alloys, the DSC and XRD analyses were carried out on the alloy, as displayed in Fig. 1 and 2. Fig. 1 shows that the endothermic and exothermic peaks of the reversible MT for alloys can be observed in the heating and cooling processes. It is seen that the MT temperature gradually increases with the increase of B content. For Ni-Mn-based Heusler alloys, the electron

concentration (e/a) is an important parameter for assessing the MT temperature. In general, the larger e/a corresponds to a higher MT temperature [7, 9]. To further analyze the e/a of the alloys, the compositions of the matrix and second phase were determined by EDS and wavelength dispersive spectrum (WDS), as displayed in Table 1. The primary reason for the change of e/a is caused by the formation of a second phase with doping of B. The increase of e/a for the matrix as a result of the B-rich second phase that formed, which leads to an increase in the MT temperature. Besides, the phase transformation entropy change ($\otimes S_{tr}$) of the $(\text{Ni}_{37}\text{Co}_{13}\text{Mn}_{34}\text{Ti}_{16})_{100-x}\text{B}_x$ alloys increases with the increasing B content, the reason for this phenomenon will be discussed later in Section 3.3.

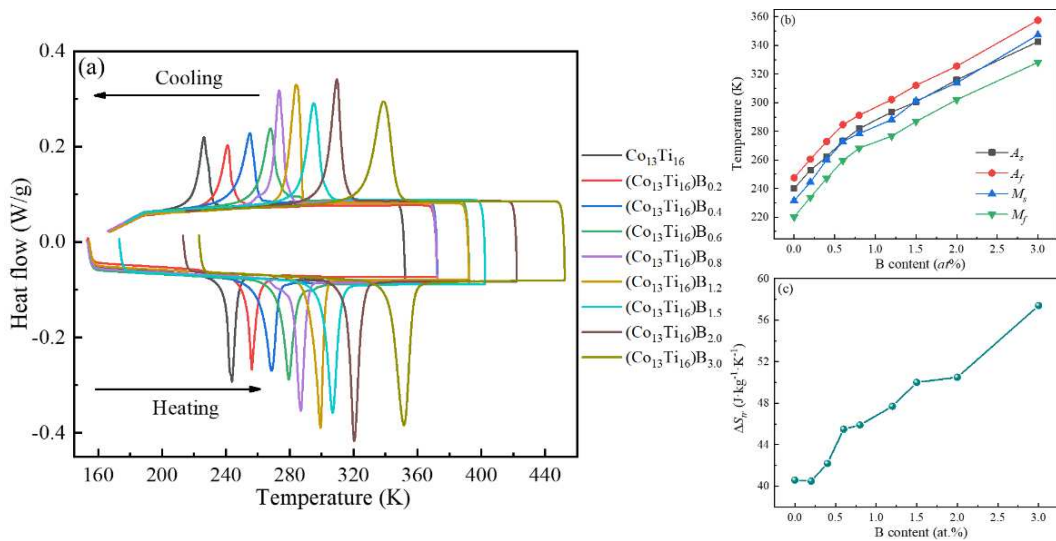


Fig. 1. (a) DSC curves of the martensitic transformation for $(\text{Ni}_{37}\text{Co}_{13}\text{Mn}_{34}\text{Ti}_{16})_{100-x}\text{B}_x$ alloys; (b) and (c) show the reversible martensitic transformation temperature (M_s , M_f , A_s , and A_f) and the transformation entropy change $\otimes S_{tr}$, respectively, as a function of B content.

Table 1. Actual compositions of the matrix and second phases for $(\text{Ni}_{37}\text{Co}_{13}\text{Mn}_{34}\text{Ti}_{16})_{100-x}\text{B}_x$ alloys.

B content	Matrix composition (at.%)				e/a	Second phase (at.%)				
	Ni	Co	Mn	Ti		Ni	Co	Mn	Ti	B
$\text{Co}_{13}\text{Ti}_{16}$	36.48	13.30	33.89	16.33	7.87	4.84	2.37	5.47	87.32	—
$(\text{Co}_{13}\text{Ti}_{16})\text{B}_{0.2}$	36.93	13.02	33.90	16.17	7.88	0.55	0.19	1.06	31.38	66.82
$(\text{Co}_{13}\text{Ti}_{16})\text{B}_{0.4}$	36.88	13.07	34.18	15.87	7.89	0.99	0.31	0.96	30.84	66.90
$(\text{Co}_{13}\text{Ti}_{16})\text{B}_{0.6}$	37.04	13.29	33.81	15.86	7.90	1.50	1.05	2.41	27.03	68.01
$(\text{Co}_{13}\text{Ti}_{16})\text{B}_{0.8}$	37.15	13.12	34.02	15.71	7.91	2.34	1.34	2.93	26.19	67.20
$(\text{Co}_{13}\text{Ti}_{16})\text{B}_{1.2}$	37.29	13.04	34.25	15.42	7.92	2.36	1.43	3.17	27.27	65.77
$(\text{Co}_{13}\text{Ti}_{16})\text{B}_{1.5}$	37.46	13.06	34.18	15.30	7.93	2.38	0.91	2.93	28.53	65.25
$(\text{Co}_{13}\text{Ti}_{16})\text{B}_{2.0}$	37.63	12.99	34.27	15.11	7.94	2.44	1.29	2.12	28.68	65.47
$(\text{Co}_{13}\text{Ti}_{16})\text{B}_{3.0}$	37.82	13.13	34.39	14.66	7.96	2.06	1.34	2.07	29.27	67.26

Fig. 2 presents the secondary electron images for the $\text{Co}_{13}\text{Ti}_{16}$, $(\text{Co}_{13}\text{Ti}_{16})\text{B}_{0.8}$, $(\text{Co}_{13}\text{Ti}_{16})\text{B}_{1.5}$, and $(\text{Co}_{13}\text{Ti}_{16})\text{B}_{3.0}$ alloys. It can be seen that there are two types of second phase in the $(\text{Ni}_{37}\text{Co}_{13}\text{Mn}_{34}\text{Ti}_{16})_{100-x}\text{B}_x$ alloys. When the B content increases, the amount of the Ti-rich second phase decreases, and the amount of the B-rich second phase increases. The amount of Ti-rich second

phase in the original $\text{Co}_{13}\text{Ti}_{16}$ alloy reduces due to the formation of the B-rich second phase with a B to Ti ratio of about 2 to 1 after B doping.

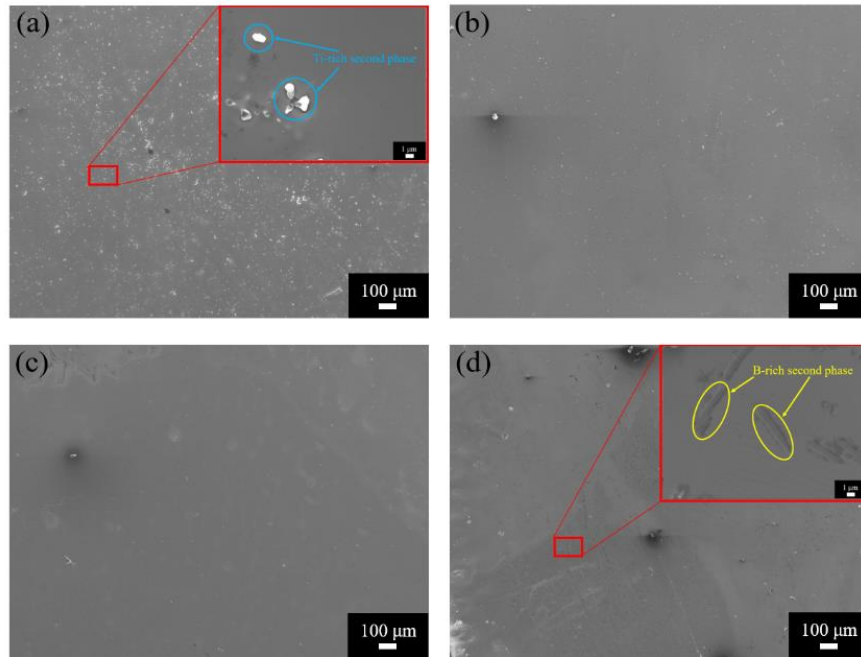


Fig. 2. Second electron images of $\text{Co}_{13}\text{Ti}_{16}$, $(\text{Co}_{13}\text{Ti}_{16})\text{B}_{0.8}$, $(\text{Co}_{13}\text{Ti}_{16})\text{B}_{1.5}$, and $(\text{Co}_{13}\text{Ti}_{16})\text{B}_{3.0}$ alloys at RT.

To ascertain the crystal structure of $(\text{Ni}_{37}\text{Co}_{13}\text{Mn}_{34}\text{Ti}_{16})_{100-x}\text{B}_x$ ($x = 0\sim 3$) alloys, the powder XRD experiments were conducted at RT and the patterns were shown in Fig. 3. As indicated from the diffraction peaks, the structure of B2 austenite and 5-layer modulated (5M) martensite can be indexed. The austenite diffraction peaks correspond with B2 crystal structure when the B content is less than 1.2 at.%, confirming that the MT temperature is below RT. With a continued increase in the B content, the diffraction peaks of 5M martensite emerges, suggesting a shift in MT temperature to higher temperatures. The XRD results are in good agreement with the DSC data.

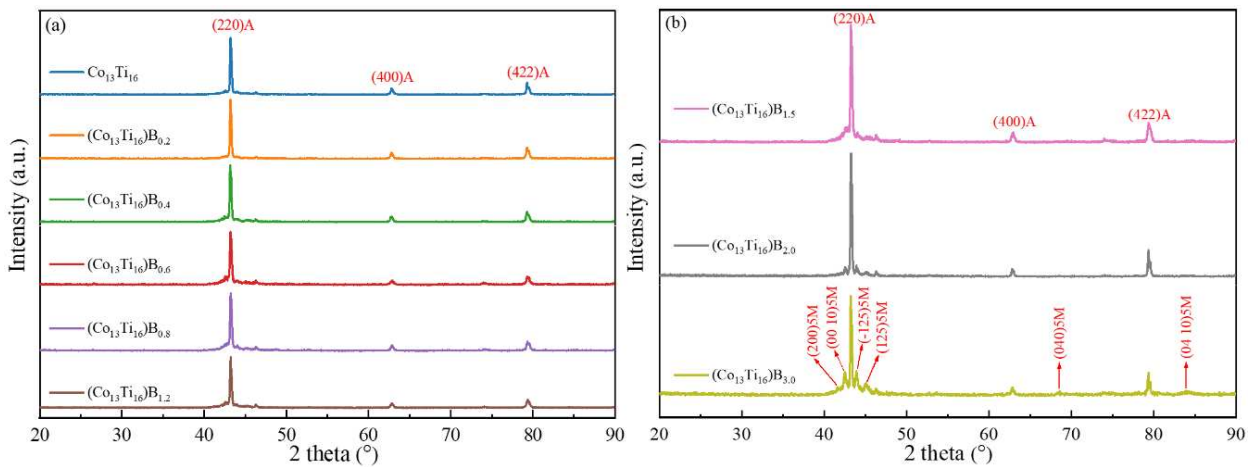


Fig. 3. XRD patterns of $(\text{Ni}_{37}\text{Co}_{13}\text{Mn}_{34}\text{Ti}_{16})_{100-x}\text{B}_x$ ($x = 0\sim 3$) alloys at RT.

To further determine the crystal structure, the $(\text{Co}_{13}\text{Ti}_{16})\text{B}_{1.5}$ alloy with MT temperature near RT was selected for TEM investigation, and the results are presented in Fig. 4. It is seen that both

austenite and martensite exist in the alloy at RT, there is an obvious coherent phase boundary between the austenitic and martensitic phases. Fig. 4(a) displays the high-resolution TEM image showing the interface between the austenite and martensite, the inset shows the bright field image (BFI) of the interface. The corresponding selected area electron diffraction (SAED) patterns of austenite and martensite are shown in Fig. 4(b). The SAED patterns of the B2 cubic structure along the [111] zone axis and the 5M monoclinic structure along the [210] zone axis can be indexed. This is in good agreement with the crystal structures measured by powder XRD patterns.

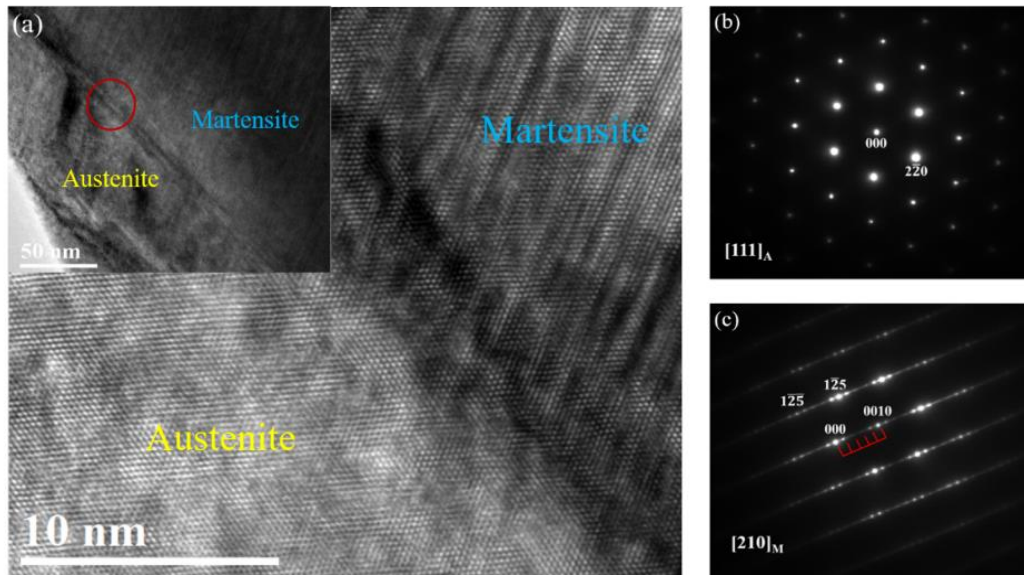


Fig. 4. (a) High-resolution TEM image at the interface of the austenite and martensite, the inset shows the BFI of the interface; selected area electron diffraction patterns of austenite (b) and martensite (c).

3.2. Mechanical properties

Fig. 5 shows the stress-strain curves and SEM micrographs of the fractured surface for the $(\text{Ni}_{137}\text{Co}_{13}\text{Mn}_{34}\text{Ti}_{16})_{100-x}\text{B}_x$ ($x = 0\sim 3$) alloys at RT. Fig. 5(a) indicates that the mechanical properties significantly enhance with increasing B content. To examine the fracture mechanism, Fig. 6(b)-(e) display the fracture surface of the $\text{Co}_{13}\text{Ti}_{16}$, $(\text{Co}_{13}\text{Ti}_{16})\text{B}_{0.8}$, $(\text{Co}_{13}\text{Ti}_{16})\text{B}_{1.5}$ and $(\text{Co}_{13}\text{Ti}_{16})\text{B}_{3.0}$ alloys at 298 K observed by SEM. It can be seen that the fracture mode of the alloys changes from a single intergranular fracture to a predominantly transgranular fracture after doping with B. Intergranular fracture of boron-free alloys is owing to the weak grain boundaries of Ni-Mn-based Heusler alloys [9, 17]. In contrast, the fracture mode of B-doped alloys changes to transgranular fracture. This is one indication of boron microalloying resulting in grain boundary strengthening. The change in fracture mechanism results in the improvement of the mechanical properties of the alloys.

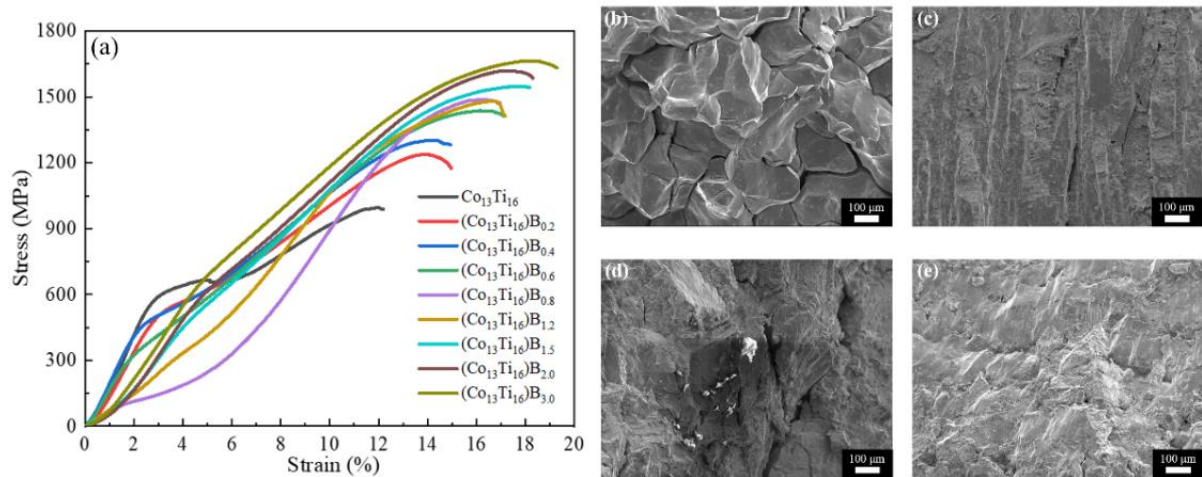


Fig. 5. (a) Stress-strain curves for $(\text{Ni}_{37}\text{Co}_{13}\text{Mn}_{34}\text{Ti}_{16})_{100-x}\text{B}_x$ alloys at 290 K. (b), (c), (d), and (e) SEM micrograph of fractured surface for B0, B0.8, B1.5, and B3 alloys at 298 K.

To further investigate the essential reasons for the improved mechanical properties of the alloys after B doping, the backscatter electron (BSE) and TEM results of the $(\text{Ni}_{37}\text{Co}_{13}\text{Mn}_{34}\text{Ti}_{16})_{100-x}\text{B}_x$ ($x = 0\sim 3$) alloys at RT were analyzed. The BSE images of the $\text{Co}_{13}\text{Ti}_{16}$, $(\text{Co}_{13}\text{Ti}_{16})\text{B}_{0.8}$, $(\text{Co}_{13}\text{Ti}_{16})\text{B}_{1.2}$, and $(\text{Co}_{13}\text{Ti}_{16})\text{B}_{3.0}$ alloys are shown in Fig. 6. With the increase of B content, the microstructure of the alloys changes from single austenite to the coexistence of martensitic and austenitic phases, and then to a single martensite, which is consistent with the above-mentioned DSC and XRD results. Fig. 6(a) and (b) show that the introduction of B facilitates the refinement of the grains. Due to the refinement of the grains, the stress between neighboring grains becomes smaller, which leads to a reduction in stress concentration at grain boundaries and avoids the formation of cracks. This is one reason for the significant improvement in mechanical properties. Besides, without doping B, the second phase of the $\text{Co}_{13}\text{Ti}_{16}$ alloy is a randomly distributed spot-shaped Ti-rich second phase. A strip-shaped B-rich second phase is formed along the grain boundaries with the introduction of B, and the observed results are in agreement with those obtained in recent literature using three-dimensional atom probe tomography (3DAPT) [17]. The B-rich second phase can promote the strengthening of grain boundaries by forming the nanosized NiBH cluster to trap hydrogen and further suppress hydrogen embrittlement [17, 30]. The above results indicate that B doping results in both grain refinement and grain boundary strengthening mechanisms to improve the mechanical properties.

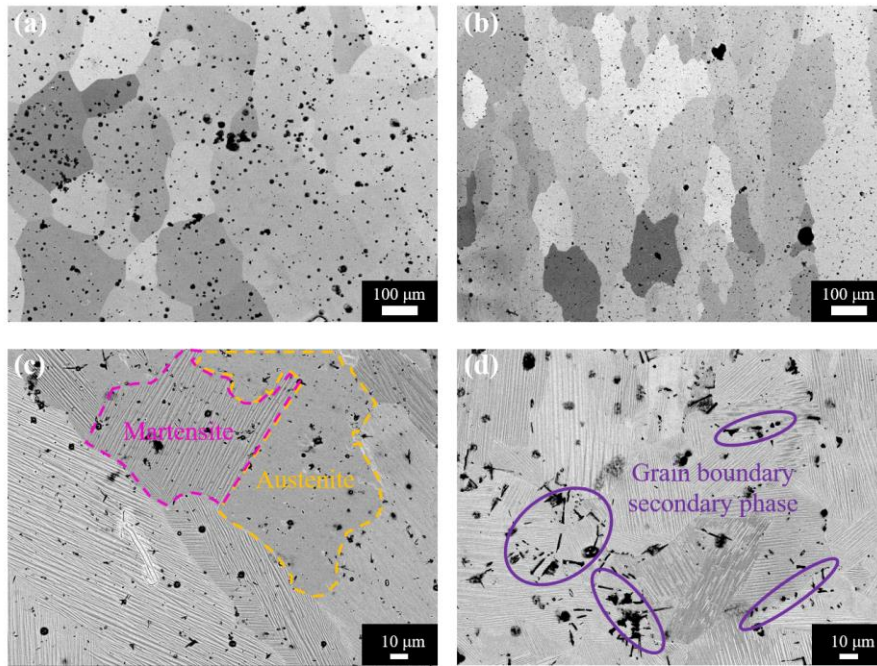


Fig. 6. BSE images of $\text{Co}_{13}\text{Ti}_{16}$, $(\text{Co}_{13}\text{Ti}_{16})\text{B}_{0.8}$, $(\text{Co}_{13}\text{Ti}_{16})\text{B}_{1.2}$, and $(\text{Co}_{13}\text{Ti}_{16})\text{B}_{3.0}$ alloys at RT.

The second phase changes from $(\text{Ni,Mn})_3\text{Ti}$ in the ternary Ni-Mn-Ti alloy to the Ti-rich second phase in the Ni-Co-Mn-Ti alloys [31-33] after Co doping. To investigate whether the Ti-rich second phase in the Ni-Co-Mn-Ti alloy forms a second phase strengthening mechanism with the matrix, a TEM study of the Ti-rich second phase in the $(\text{Co}_{13}\text{Ti}_{16})\text{B}_{1.5}$ alloy was carried out. Fig. 7(a) exhibits a bright field image in which both matrix and the Ti-rich second phase are presented. The structure of the Ti-rich second phase can be seen in Fig. 7(b) as a hexagonal crystal. Fig. 7(c) displays the high-resolution image of the interface region. It shows that the interface between the matrix and the Ti-rich second phase is incoherent with a large lattice misfit. This indicates that the Ti-rich second phase has little contribution to the mechanical properties. Therefore, the enhancement of the mechanical properties of the $(\text{Ni}_{37}\text{Co}_{13}\text{Mn}_{34}\text{Ti}_{16})_{100-x}\text{B}_x$ ($x = 0\sim 3$) alloys mainly derives from the grain refinement and grain boundary strengthening caused by the B doping.

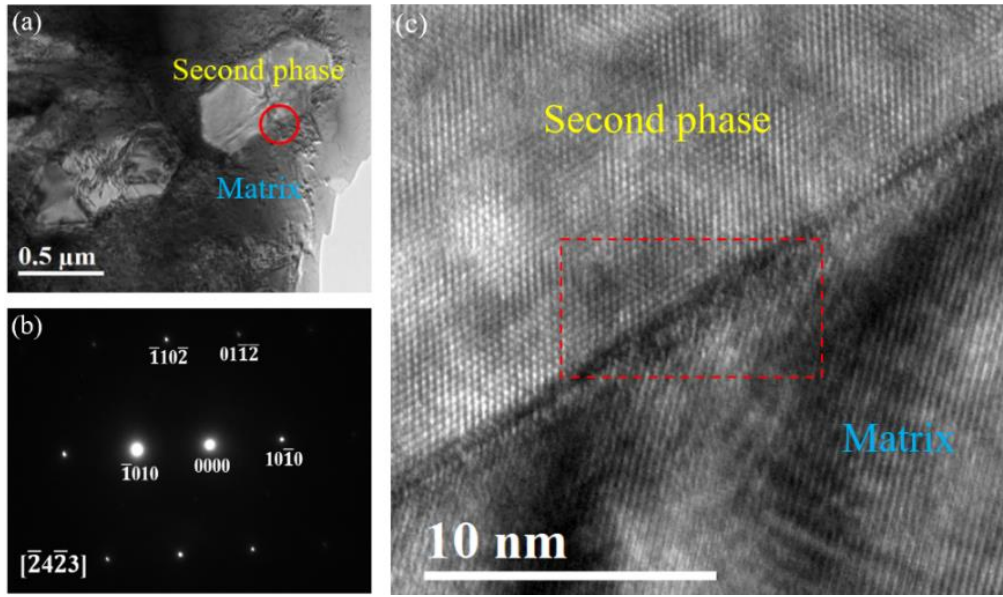


Fig. 7. (a) BFI of the matrix and Ti-rich second phase for $(\text{Co}_{13}\text{Ti}_{16})\text{B}_{1.5}$ alloy. (b) Selected area electron diffraction patterns of Ti-rich second phase. (c) High-resolution TEM image at the interface of the matrix and Ti-rich second phase.

3.3. Magnetic properties

The M-T curves of the $(\text{Ni}_{37}\text{Co}_{13}\text{Mn}_{34}\text{Ti}_{16})_{100-x}\text{B}_x$ ($x = 0\sim 3$) alloys under the magnetic fields of 0.05 T and 5 T are demonstrated in Fig. 8. It can be seen from the figure that the magnetization difference (ΔM) changes significantly during the magnetic field induced MT, which is due to the transformation from ferromagnetic austenite to weak magnetic martensite. Besides, the MT temperature (T_M) of the alloys changes markedly with the increase of the doped B content, whereas the degree of change in T_C is slight, which leads to a decrease in the difference between T_C and T_M of the alloys. It has been reported in the literature that in Ni-Mn-based ferromagnetic shape memory alloys, $\otimes S_{tr}$ is closely related to the difference between T_C and T_M [34, 35]. The closer the T_M is to the T_C , the negative contribution of ΔS_m weakens and therefore $\otimes S_{tr}$ increases. This also explains the increase in $\otimes S_{tr}$ of the alloys with increasing B content in Section 3.1.

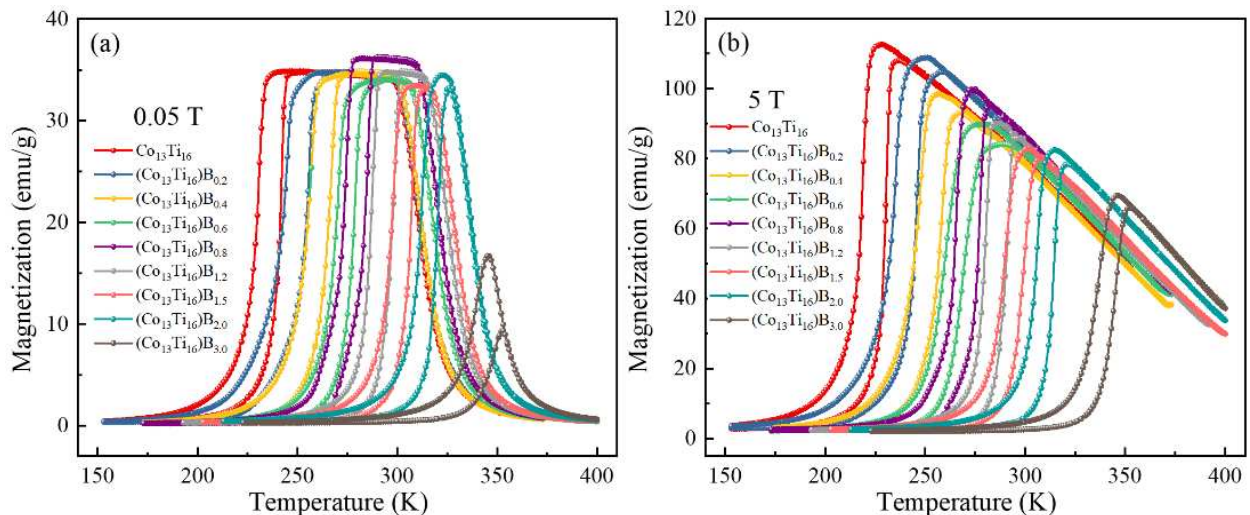


Fig. 8. M-T curves of the $(\text{Ni}_{37}\text{Co}_{13}\text{Mn}_{34}\text{Ti}_{16})_{100-x}\text{B}_x$ ($x = 0\sim 3$) alloys

To investigate the effect of B doping on the magnetic properties, the M-H curves of $\text{Co}_{13}\text{Ti}_{16}$ and $(\text{Co}_{13}\text{Ti}_{16})\text{B}_{0.8}$ alloys were measured under the magnetic field changes of 7 T, as presented in Fig. 9. To avoid misestimating ΔS_m caused by retained austenite, a discontinuous heating protocol method [36] was performed at different temperatures. It is seen from Fig. 9 (a) and (b) that both the alloys have a significant metamagnetic transition behavior in the MT temperature interval, indicating that the magnetic field induced a reversible MT. Based on the results of the M-H curves, the maximum ΔS_m of $\text{Co}_{13}\text{Ti}_{16}$ and $(\text{Co}_{13}\text{Ti}_{16})\text{B}_{0.8}$ alloys stimulated by 7 T magnetic field are $40.1 \text{ J}\cdot\text{kg}^{-1}\cdot\text{K}^{-1}$ and $40.9 \text{ J}\cdot\text{kg}^{-1}\cdot\text{K}^{-1}$ calculated by Maxwell equation [6, 37], respectively, as shown in Fig. 9(c) and (d). The above results demonstrated that doping with a small amount of B not only improved the mechanical properties significantly but also did not reduce the MCE of the alloys. In addition, the B doping can also adjust the MT temperature to RT, and the $(\text{Co}_{13}\text{Ti}_{16})\text{B}_{0.8}$ alloy studied in this section simultaneously achieves excellent mechanical properties and large MCE near RT.

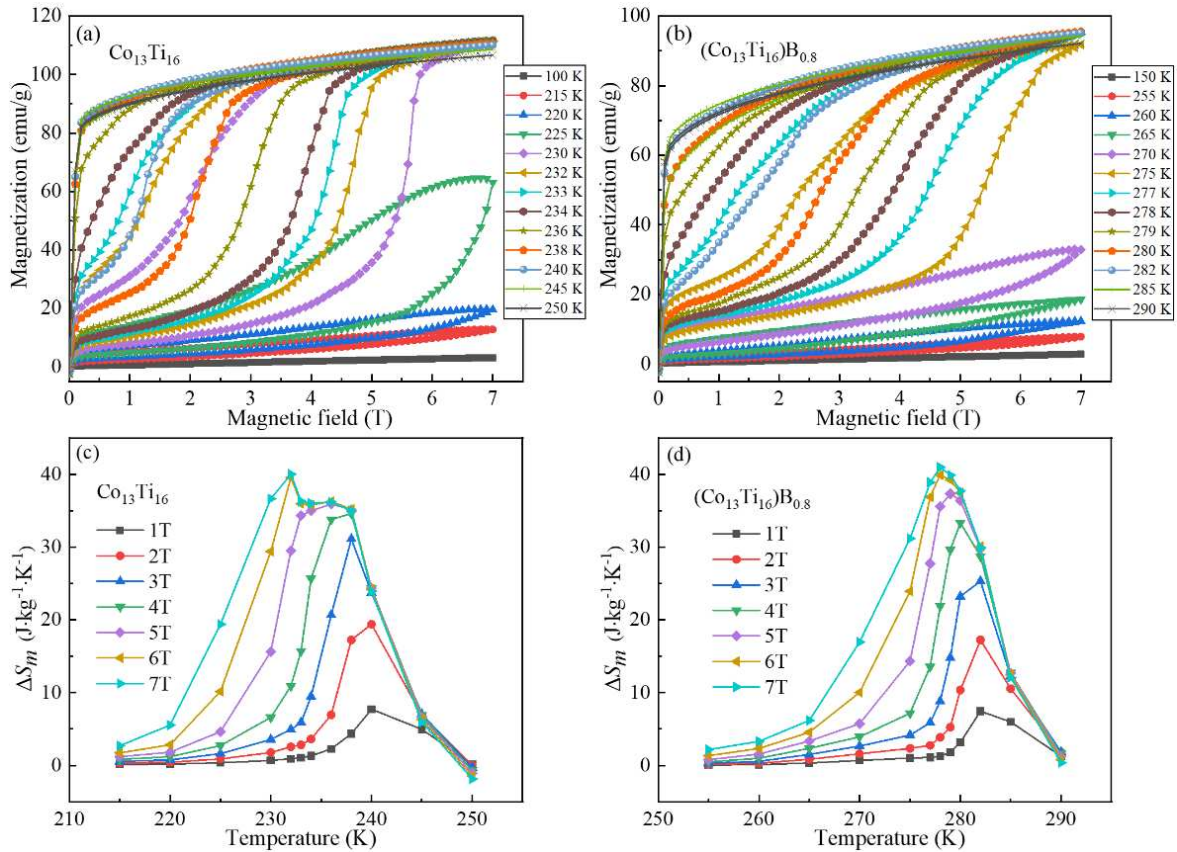


Fig. 9. (a) M-H curves of $\text{Co}_{13}\text{Ti}_{16}$ alloy at selected temperatures around MT. (b) ΔS_m as a function of temperature under different magnetic field changes of $\text{Co}_{13}\text{Ti}_{16}$ alloy. (c) M-H curves of $(\text{Co}_{13}\text{Ti}_{16})\text{B}_{0.8}$ alloy at selected temperatures around MT. (d) ΔS_m as a function of temperature under different magnetic field changes of $(\text{Co}_{13}\text{Ti}_{16})\text{B}_{0.8}$ alloy.

To describe more visually the effect of B content on the MT temperature and the magnetostructural coupling in the $(\text{Ni}_{37}\text{Co}_{13}\text{Mn}_{34}\text{Ti}_{16})_{100-x}\text{B}_x$ ($x = 0\sim 3$) alloys, the magnetic and structural phase diagram was plotted and shown in Fig. 10. As can be found from the figure, the

magnetostructural coupling phenomenon disappears when B content exceeds 2.0 at.%. It should be noted that the T_M is slightly lower than T_C when B content is around 1.5 at.%. It is conducive to realize the combined caloric effects when the MT temperature is connected with the magnetic transition temperature.

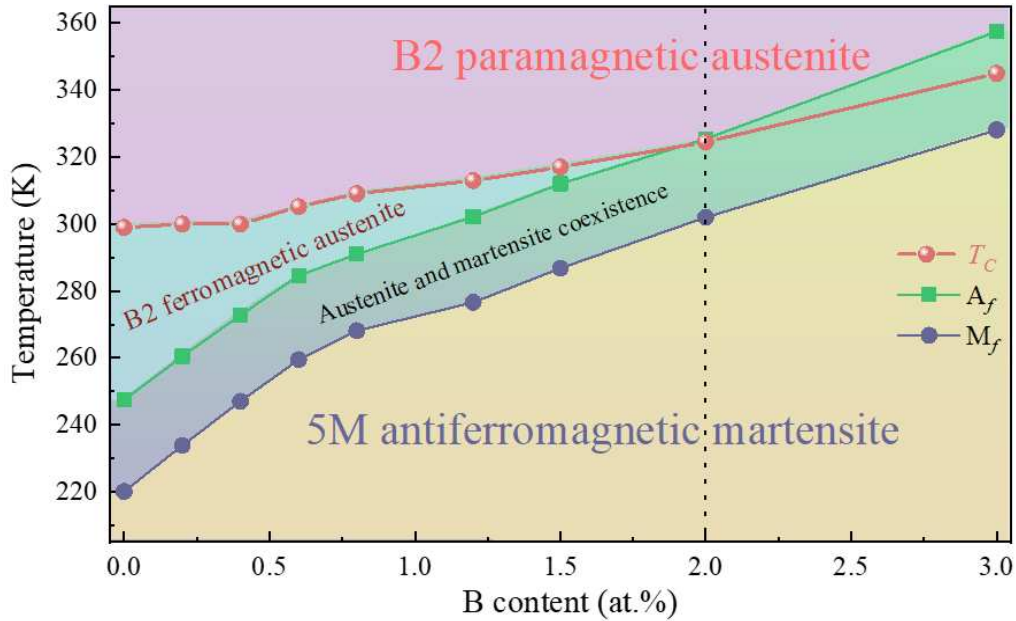


Fig. 10. Magnetic and structural phase diagram of $(\text{Ni}_{37}\text{Co}_{13}\text{Mn}_{34}\text{Ti}_{16})_{100-x}\text{B}_x$ ($x = 0\sim 3$) alloys.

3.4. Combined caloric effects of the $(\text{Ni}_{37}\text{Co}_{13}\text{Mn}_{34}\text{Ti}_{16})_{98.5}\text{B}_{1.5}$ alloy

Based on the above magnetic and structural phase diagram, the $(\text{Co}_{13}\text{Ti}_{16})\text{B}_{1.5}$ alloy with a slightly lower T_M than T_C was selected as the research sample for the combined caloric effects study. Fig. 11(a) and (b) present the M-H curves measured using the discontinuous heating protocol method under a 7 T magnetic field and ΔS_m calculated by the Maxwell equation. The alloy shows a significant metamagnetic transition behavior, and the maximum ΔS_m of $33.4 \text{ J}\cdot\text{kg}^{-1}\cdot\text{K}^{-1}$ and $40.3 \text{ J}\cdot\text{kg}^{-1}\cdot\text{K}^{-1}$ can be obtained upon the magnetic field of 5 T and 7 T, respectively. Fig. 11(c) illustrates the ΔS_m comparison between the present alloy and some typical Ni-Mn-based MCE materials under the 5 T magnetic field. It can be seen that the ΔS_m value in the present alloy is larger than most of the reported Ni-Mn-based materials [27, 38-55]. Meanwhile, the fracture compressive strength and strain of the $(\text{Co}_{13}\text{Ti}_{16})\text{B}_{1.5}$ alloy at 290 K reached 1553 MPa and 17.7%, respectively, well beyond those in many Ni-Mn-based alloys, e.g., the $\text{Ni}_{51.5}\text{Mn}_{33}\text{In}_{15.5}$ alloy (i.e., $\sim 522 \text{ MPa}$, $\sim 2.4\%$) [9], the $\text{Ni}_{43}\text{Co}_6\text{Mn}_{40}\text{Sn}_{11}$ alloy (i.e., $\sim 716 \text{ MPa}$, $\sim 6.3\%$) [20], the $\text{Ni}_{45}\text{Mn}_{37}\text{In}_{13}\text{Co}_5$ alloy (i.e., $\sim 155 \text{ MPa}$,

~2.2%) [56], the $\text{Ni}_{50}\text{Mn}_{31.5}\text{Ti}_{18.5}$ alloy (i.e., ~1100 MPa, ~13.0%) [23], and the $\text{Ni}_{50}\text{Mn}_{35}\text{In}_{15}$ alloy (i.e., ~847 MPa, ~11.3%) [21].

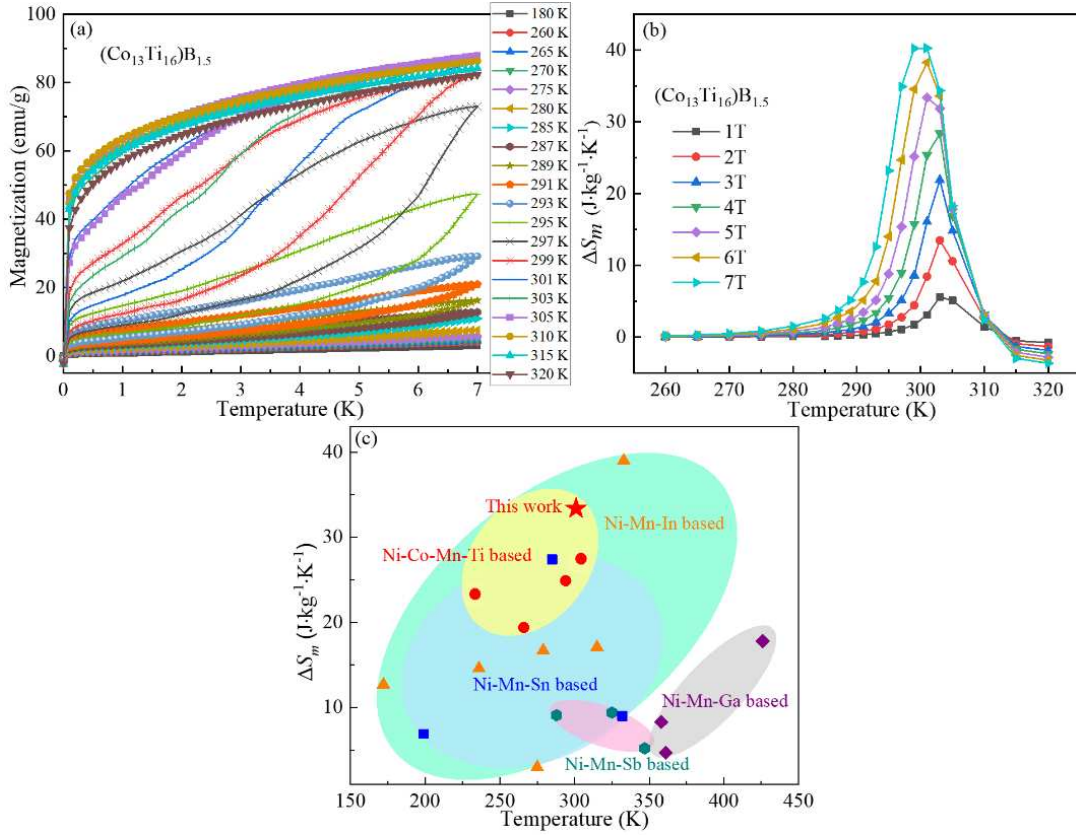


Fig. 11. (a) M-H curves of $(\text{Co}_{13}\text{Ti}_{16})\text{B}_{1.5}$ alloy at selected temperatures around martensitic transformation; (b) ΔS_m as a function of temperature under different magnetic field changes of $(\text{Co}_{13}\text{Ti}_{16})\text{B}_{1.5}$ alloy. (c) ΔS_m for some typical Ni-Mn-based MCE materials under field change of 5 T.

Fig. 12(a) and (b) show the DSC curves of the $(\text{Co}_{13}\text{Ti}_{16})\text{B}_{1.5}$ alloy for 50 heating/cooling cycles and the M-T curve under 0.05 T magnetic field, respectively. It is seen that the endothermic and exothermic peaks during thermal cycling have coincided well, indicating that the alloy has good cyclic stability of the MT. Moreover, it can also be seen from the M-T curve that the T_M and T_C of the $(\text{Co}_{13}\text{Ti}_{16})\text{B}_{1.5}$ alloy are around 320 K. Therefore, the temperature above 320 K is selected for the elastocaloric experiments to weaken the negative contribution of ΔS_m to obtain a larger eCE.

Fig. 12(c) displays the compressive stress-strain superelastic curves in the temperature range of 323 K to 363 K with the 7% strain. The superelastic curves of the alloy have a residual strain of about 2% at 323 K. This is because the T_M is very close to the testing temperature and more residual martensite is produced during the stress-induced MT. As the temperature increases, the residual strain of stress-induced reversible MT gradually decreases, with a residual strain of about 0.8% at 353 K and 363 K. Fig. 12(d) presents the elastocaloric ΔT_{ad} of the $(\text{Co}_{13}\text{Ti}_{16})\text{B}_{1.5}$ alloy at different temperatures. At a high strain rate of $5.6 \times 10^{-1} \text{ s}^{-1}$, with the temperature increasing from 323 K to 353

K, the elastocaloric ΔT_{ad} increases from 11.2 K to 18.0 K during loading and from -5.9 K to -11.9 K during unloading process. This phenomenon is because the closer the testing temperature is to the T_C , the weaker the negative contribution from ΔS_m and thus the more pronounced eCE of the alloy.

Besides, the elastocaloric ΔT_{ad} of loading is significantly higher than that of unloaded, which is caused by the residual strain and the high strain rate unloading that drastically reduces the volume fraction of MT. The elastocaloric ΔT_{ad} decreases when the temperature is 363 K. This is because the high temperature decreases the transformation strain of the alloy, which in turn reduces the phase change volume fraction of the alloy [21, 57]. The above results indicate that the present alloy exhibits a prominent eCE.

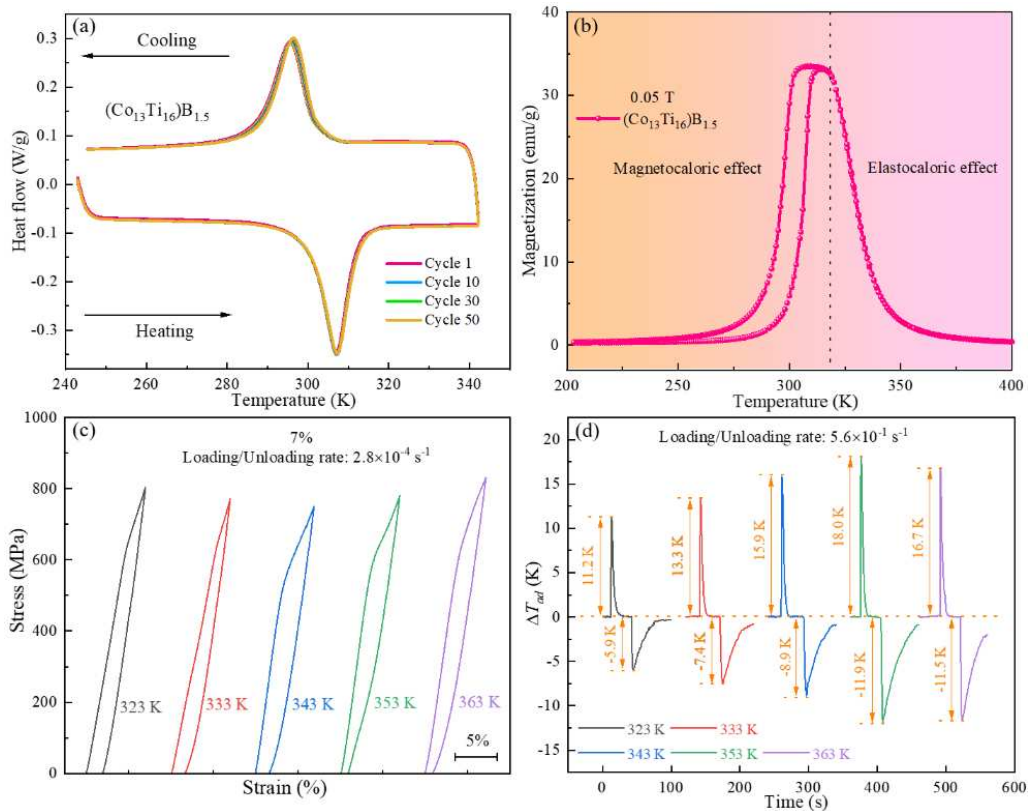


Fig. 12. (a) DSC curves during thermal cycling across martensitic transformation for (Co₁₃Ti₁₆)B_{1.5} alloy. (b) M-T curve on heating and cooling under 0.05 T field. (c) Compressive superelastic responses at various temperatures. (d) Time dependence of ΔT_{ad} on loading/unloading measured at various temperatures.

The (Co₁₃Ti₁₆)B_{1.5} alloy exhibits large MCE and eCE, as well as excellent mechanical properties, indicating that the alloy has great potential in the field of solid-state refrigeration. Fig. 13 shows the temperature dependence of magnetocaloric ΔS_m and elastocaloric ΔT_{ad} of alloy. It can be seen from the figure that the working temperature interval between MCE and eCE is connected. Therefore, the combination of these two types of caloric effects can form the combined caloric effect, resulting in a wide working temperature region of more than 90 K near RT.

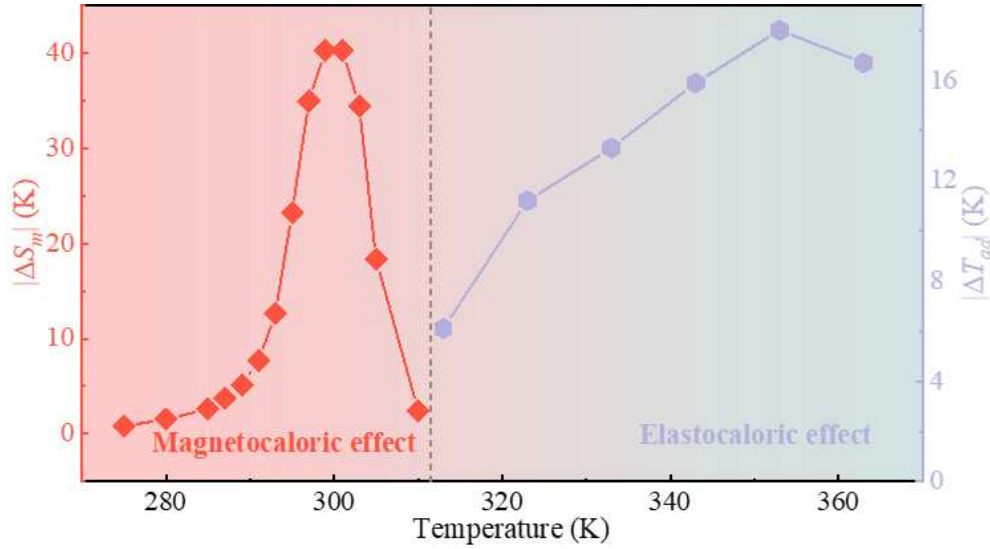


Fig. 13. Temperature dependence of combined caloric effect for $(\text{Co}_{13}\text{Ti}_{16})\text{B}_{1.5}$ alloy.

4. Conclusions

In summary, the MT, mechanical properties, MCE, eCE, and combined caloric effect of the $(\text{Ni}_{37}\text{Co}_{13}\text{Mn}_{34}\text{Ti}_{16})_{100-x}\text{B}_x$ ($x = 0\sim 3$) alloys were systematically investigated. An increase in B content will reduce the difference between T_C and T_M of the alloys to weaken the negative magnetic contribution and thus increase the ΔS_{tr} . After doping with B, the grain refinement and grain boundary strengthening will be formed to improve the mechanical properties. Besides, B doping can tune the functional behavior, which is conducive to achieve the combined caloric effect. The prepared $(\text{Ni}_{37}\text{Co}_{13}\text{Mn}_{34}\text{Ti}_{16})_{98.5}\text{B}_{1.5}$ as-cast alloy has a fracture compressive strength and strain of 1553 MPa and 17.7% at RT, respectively. The maximum ΔS_m of the alloy is $40.3 \text{ J}\cdot\text{kg}^{-1}\cdot\text{K}^{-1}$ under the magnetic field changes of 7 T. In addition, the alloy can also yield a large elastocaloric ΔT_{ad} of 18.0 K. The above results suggest that doping of B in Ni-Co-Mn-Ti alloys can not only improve the mechanical properties greatly but also broaden the working temperature range by achieving combined caloric effect near RT.

Acknowledgments

This work is supported by the National Natural Science Foundation of China (Grant No. 51771044), the Fundamental Research Funds for the Central Universities (No. N2223025), the Performance subsidy fund for Key Laboratory of Dielectric and Electrolyte Functional Material Hebei (No. 22567627H), and Programme of Introducing Talents of Discipline Innovation to Universities 2.0 (the 111 Project of China 2.0, No. BP0719037).

Author contributions

Zuo L and Bai J conceived and coordinated the project, and were responsible for the infrastructure and project direction. Guan ZQ and Gu JL conducted the theoretical calculations. Zhang YD, Esling C, and Zhao X contributed to data analysis and interpretation. Guan ZQ wrote the manuscript. All authors contributed to the general discussion.

Conflict of interest

The authors declare that they have no known competing financial interests or personal relationships that could have appeared to influence the work reported in this paper.

References

- [1] D.Y. Cong, S. Roth, L. Schultz, Magnetic properties and structural transformations in Ni-Co-Mn-Sn multifunctional alloys, *Acta Mater.* 60 (2012) 5335–5351.
- [2] X. Moya, S. Kar-Narayan, N.D. Mathur, Caloric materials near ferroic phase transitions, *Nat. Mater.* 13 (2014) 439–450.
- [3] R. Kainuma, Y. Imano, W. Ito, Y. Sutou, H. Morito, S. Okamoto, O. Kitakami, K. Oikawa, A. Fujita, T. Kanomata, K. Ishida, Magnetic-field-induced shape recovery by reverse phase transformation, *Nature* 439 (2006) 957–960.
- [4] V. Franco, J.S. Blázquez, J.J. Ipus, J.Y. Law, L.M. Moreno-Ramírez, A. Conde, Magnetocaloric effect: From materials research to refrigeration devices, *Prog. Mater. Sci.* 93 (2018) 112–232.
- [5] J. Liu, T. Gottschall, K.P. Skokov, J.D. Moore, O. Gutfleisch, Giant magnetocaloric effect driven by structural transitions, *Nat. Mater.* 11 (2012) 620–626.
- [6] T. Krenke, E. Duman, M. Acet, E.F. Wassermann, X. Moya, L. Manosa, A. Planes, Inverse magnetocaloric effect in ferromagnetic Ni-Mn-Sn alloys, *Nat. Mater.* 4 (2005) 450–454.
- [7] H.N. Bez, A.K. Pathak, A. Biswas, N. Zarkevich, V. Balema, Y. Mudryk, D.D. Johnson, V.K. Pecharsky, Giant enhancement of the magnetocaloric response in Ni-Co-Mn-Ti by rapid solidification, *Acta Mater.* 173 (2019) 225–230.
- [8] C. Liu, D. Li, Z.B. Li, B. Yang, H.L. Yan, J.R. Li, Z. Li, X. Zhao, L. Zuo, Large elastocaloric effect in a Heusler-type $\text{Co}_{50}\text{V}_{35}\text{Ga}_{14}\text{Ni}_1$ polycrystalline alloy, *Appl. Phys. Lett.* 118 (2021) 103904.
- [9] Z. Yang, D.Y. Cong, X.M. Sun, Z.H. Nie, Y.D. Wang, Enhanced cyclability of elastocaloric effect in boron-microalloyed Ni-Mn-In magnetic shape memory alloys, *Acta Mater.* 127 (2017) 33–42.
- [10] Y.J. Huang, Q.D. Hu, N.M. Bruno, J.H. Chen, I. Karaman, J.H. Ross, Jr., J.G. Li, Giant elastocaloric effect in directionally solidified Ni-Mn-In magnetic shape memory alloy, *Scr. Mater.* 105 (2015) 42–45.
- [11] J. Cui, Y.M. Wu, J. Muehlbauer, Y. Hwang, R. Radermacher, S. Fackler, M. Wuttig, I. Takeuchi, Demonstration of high efficiency elastocaloric cooling with large ΔT using NiTi wires, *Appl. Phys. Lett.* 101 (2012) 073904.
- [12] A.S. Mischenko, Q. Zhang, J.F. Scott, R.W. Whatmore, N.D. Mathur, Giant Electrocaloric Effect in Thin-Film $\text{PbZr}_{0.95}\text{Ti}_{0.05}\text{O}_3$, *Science* 311 (2006) 1270–1271.
- [13] P. Lloveras, E. Stern-Taulats, M. Barrio, J.L. Tamarit, S. Crossley, W. Li, V. Pomjakushin, A. Planes, L.

Manosa, N.D. Mathur, X. Moya, Giant barocaloric effects at low pressure in ferroelectric ammonium sulphate, *Nat. Commun.* 6 (2015) 8801.

[14] H.W. Liu, Z. Li, Y.L. Zhang, Z.T. Ni, K. Xu, Y.S. Liu, A large barocaloric effect associated with paramagnetic martensitic transformation in $\text{Co}_{50}\text{Fe}_{2.5}\text{V}_{31.5}\text{Ga}_{16}$ quaternary Heusler alloy, *Scr. Mater.* 177 (2020) 1–5.

[15] A. Aznar, P. Lloveras, J.Y. Kim, E. Stern-Taulats, M. Barrio, J.L. Tamarit, C.F. Sanchez-Valdes, J.L. Sanchez Llamazares, N.D. Mathur, X. Moya, Giant and Reversible Inverse Barocaloric Effects near Room Temperature in Ferromagnetic $\text{MnCoGeB}_{0.03}$, *Adv. Mater.* 31 (2019) 1903577.

[16] L. Manosa, A. Planes, Materials with giant mechanocaloric effects: cooling by strength. *Adv. Mater.* 29 (2017) 1603607.

[17] Z. Yang, D.Y. Cong, Y. Yuan, Y. Wu, Z.H. Nie, R.G. Li, Y.D. Wang, Ultrahigh cyclability of a large elastocaloric effect in multiferroic phase-transforming materials, *Mater. Res. Lett.* 7 (2019) 137–144.

[18] Z.Y. Wei, E.K. Liu, J.H. Chen, Y. Li, G.D. Liu, H.Z. Luo, X.K. Xi, H.W. Zhang, W.H. Wang, G.H. Wu, Realization of multifunctional shape-memory ferromagnets in all-d-metal Heusler phases, *Appl. Phys. Lett.* 107 (2015) 022406.

[19] Y. Hu, Z. Li, B. Yang, S. Qian, W. Gan, Y. Gong, Y. Li, D. Zhao, J. Liu, X. Zhao, L. Zuo, D. Wang, Y. Du, Combined caloric effects in a multiferroic Ni-Mn-Ga alloy with broad refrigeration temperature region, *Appl. Mater.* 5 (2017), 046103.

[20] Y.H. Qu, D.Y. Cong, S.H. Li, W.Y. Gui, Z.H. Nie, M.H. Zhang, Y. Ren, Y.D. Wang, Simultaneously achieved large reversible elastocaloric and magnetocaloric effects and their coupling in a magnetic shape memory alloy, *Acta Mater.* 151 (2018) 41–55.

[21] Z.Z. Li, Z.B. Li, D. Li, J.J. Yang, B. Yang, Y. Hu, D.H. Wang, Y.D. Zhang, C. Esling, X. Zhao, L. Zuo, Achieving a broad refrigeration temperature region through the combination of successive caloric effects in a multiferroic $\text{Ni}_{50}\text{Mn}_{35}\text{In}_{15}$ alloy, *Acta Mater.* 192 (2020) 52–59.

[22] D.Y. Cong, W.X. Xiong, A. Planes, Y. Ren, L. Mañosa, P.Y. Cao, Z.H. Nie, X.M. Sun, Z. Yang, X.F. Hong, Y.D. Wang, Colossal Elastocaloric Effect in Ferroelastic Ni-Mn-Ti Alloys, *Phys. Rev. Lett.* 122 (2019) 255703.

[23] H.L. Yan, L.D. Wang, H.X. Liu, X.M. Huang, N. Jia, Z.B. Li, B. Yang, Y.D. Zhang, C. Esling, X. Zhao, L. Zuo, Giant elastocaloric effect and exceptional mechanical properties in an all-d-metal Ni-Mn-Ti alloy: Experimental and ab-initio studies, *Mater. Design* 184 (2019) 108180.

[24] Y. Shen, Z. Wei, W. Sun, Y. Zhang, E. Liu, J. Liu, Large elastocaloric effect in directionally solidified all-d-metal Heusler metamagnetic shape memory alloys, *Acta Mater.* 188 (2020) 677–685.

[25] S. Samanta, S. Ghosh, S. Chatterjee, K. Mandal, Large magnetocaloric effect and magnetoresistance in Fe-Co doped $\text{Ni}_{50-x}(\text{FeCo})_x\text{Mn}_{37}\text{Ti}_{13}$ all-d-metal Heusler alloys, *J. Alloy. Compd.* 910 (2022) 164929.

[26] K. Liu, X.Q. Han, K. Yu, C.C. Ma, Z.S. Zhang, Y. Song, S.C. Ma, H. Zeng, C.C. Chen, X.H. Luo, S.U. Rehman, Z.C. Zhong, Magnetic-field-induced metamagnetic reverse martensitic transformation and magnetocaloric effect in all-d-metal $\text{Ni}_{36.0}\text{Co}_{14.0}\text{Mn}_{35.7}\text{Ti}_{14.3}$ alloy ribbons, *Intermetallics* 110 (2019) 106472.

[27] K. Liu, S.C. Ma, C.C. Ma, X.Q. Han, K. Yu, S. Yang, Z.S. Zhang, Y. Song, X.H. Luo, C.C. Chen, S. U.

- Rehman, Z.C. Zhong, Martensitic transformation and giant magneto-functional properties in all-d-metal Ni-Co-Mn-Ti alloy ribbons, *J. Alloys Compd.* 790 (2019) 78–92.
- [28] Z.Y. Wei, W. Sun, Q. Shen, Y. Shen, Y.F. Zhang, E.K. Liu, J. Liu, Elastocaloric effect of all-d-metal Heusler NiMnTi(Co) magnetic shape memory alloys by digital image correlation and infrared thermography, *Appl. Phys. Lett.* 114 (2019) 101903.
- [29] Z.Q. Guan, J. Bai, Y. Zhang, J.L. Gu, X.J. Jiang, X.Z. Liang, R.K. Huang, Y.D. Zhang, C. Esling, X. Zhao, L. Zuo, Revealing essence of magnetostructural coupling of Ni-Co-Mn-Ti alloys by first-principles calculations and experimental verification *Rare Met.* 41 (2022) 1933–1947.
- [30] X.M. Huang, Y. Zhao, H.L. Yan, N. Jia, S. Tang, J. Bai, B. Yang, Z.B. Li, Y.D. Zhang, C. Esling, X. Zhao, L. Zuo, A multielement alloying strategy to improve elastocaloric and mechanical properties in Ni-Mn-based alloys via copper and boron, *Scr. Mater.* 185 (2020) 94–99.
- [31] Z.Q. Guan, J. Bai, Y. Zhang, S.D. Sun, J.L. Gu, X.Z. Liang, Y.D. Zhang, C. Esling, X. Zhao, L. Zuo, Achieved good mechanical properties and large elastocaloric effect in Ni-Mn-Ti-Cu-B alloy: experiments and first-principles calculations, *J. Alloys Compd.* 930 (2023) 167477.
- [32] F. Zhang, K. Westra, Q. Shen, I. Batashev, A. Kiecana, N. van Dijk, E. Brück, The second-order magnetic phase transition and magnetocaloric effect in all-d-metal NiCoMnTi-based Heusler alloys, *J. Alloys Compd.* 906 (2022) 164337.
- [33] Z.Q. Guan, J. Bai, Y. Zhang, J.L. Gu, Y.D. Zhang, C. Esling, X. Zhao, L. Zuo, Ultrahigh cyclic stability and giant elastocaloric effect in directionally solidified $(\text{Ni}_{50}\text{Mn}_{28}\text{Fe}_{2.5}\text{Ti}_{19.5})_{99.4}\text{B}_{0.6}$ alloy, *Scr. Mater.* 229 (2023) 115353.
- [34] V. Recarte, J.I. Pérez-Landazábal, V. Sánchez-Alarcos, V. Zablotskii, E. Cesari, S. Kustov, Entropy change linked to the martensitic transformation in metamagnetic shape memory alloys, *Acta Mater.* 60 (2012) 3168–3175.
- [35] J.M. Barandiaran, V.A. Chernenko, E. Cesari, D. Salas, P. Lazpita, J. Gutierrez, I. Orue, Magnetic influence on the martensitic transformation entropy in Ni-Mn-In metamagnetic alloy, *Appl. Phys. Lett.* 102 (2013) 071904.
- [36] Z.Z. Li, Z.B. Li, B. Yang, X. Zhao, L. Zuo, Giant low-field magnetocaloric effect in a textured $\text{Ni}_{45.3}\text{Co}_{5.1}\text{Mn}_{36.1}\text{In}_{13.5}$ alloy, *Scr. Mater.* 151 (2018) 61–65.
- [37] O. Tegus, E. Brück, K.H.J. Buschow, F.R. de Boer, Transition-metal-based magnetic refrigerants for room-temperature applications, *Nature* 415 (2002) 150–152.
- [38] J. Du, Q. Zheng, W.J. Ren, W.J. Feng, X.G. Liu, Z.D. Zhang, Magnetocaloric effect and magnetic-field-induced shape recovery effect at room temperature in ferromagnetic Heusler alloy Ni-Mn-Sb, *J. Phys. D-Appl Phys.* 40 (2007) 5523–5526.
- [39] Y. Liu, A.D. Xiao, T.Z. Yang, Z.T. Xu, X.L. Zhou, T.Y. Ma, Enhancing reversible entropy change of all-d-metal $\text{Ni}_{37.5}\text{Co}_{12.5}\text{Mn}_{35}\text{Ti}_{15}$ alloy by multiple external fields, *Scr. Mater.* 207 (2022) 114303.
- [40] Y. Li, S.Y. Huang, W.H. Wang, E.K. Liu, and L.W. Li, Ferromagnetic martensitic transformation and large magnetocaloric effect in $\text{Ni}_{35}\text{Co}_{15-x}\text{Fe}_x\text{Mn}_{35}\text{Ti}_{15}$ ($x = 2, 4, 6, 8$) alloys, *J. Appl. Phys.* 127 (2020) 233907.
- [41] J. Bai, D. Liu, J.L. Gu, X.J. Jiang, X.Z. Liang, Z.Q. Guan, Y.D. Zhang, C. Esling, X. Zhao, L. Zuo, Excellent mechanical properties and large magnetocaloric effect of spark plasma sintered Ni-Mn-In-Co alloy, *J. Mater. Sci. Technol.* 74 (2021) 46–51.

- [42] Z.Q. Guan, X.J. Jiang, J.L. Gu, J. Bai, X.Z. Liang, H.L. Yan, Y.D. Zhang, C. Esling, X. Zhao, L. Zuo, Large magnetocaloric effect and excellent mechanical properties near room temperature in Ni-Co-Mn-Ti non-textured polycrystalline alloys, *Appl. Phys. Lett.* 119 (2021), 051904.
- [43] Z.Z. Li, Z.B. Li, B. Yang, X. Zhao, L. Zuo, Giant low-field magnetocaloric effect in a textured $\text{Ni}_{45.3}\text{Co}_{5.1}\text{Mn}_{36.1}\text{In}_{13.5}$ alloy, *Scr. Mater.* 151 (2018) 61–65.
- [44] L. Huang, D.Y. Cong, L. Ma, Z.H. Nie, Z.L. Wang, H.L. Suo, Y. Ren, Y.D. Wang, Large reversible magnetocaloric effect in a Ni-Co-Mn-In magnetic shape memory alloy, *Appl. Phys. Lett.* 108 (2016), 032405.
- [45] H.H. Zhang, M.F. Qian, X.X. Zhang, S.D. Jiang, L.S. Wei, D.W. Xing, J.F. Sun, L. Geng, Magnetocaloric effect of Ni-Fe-Mn-Sn microwires prepared by melt-extraction technique, *Mater. Design* 114 (2019) 1–9.
- [46] X.X. Zhang, S.P. Miao, J.F. Sun, Magnetocaloric effect in Ni-Mn-In-Co microwires prepared by Taylor-Ulitovsky method, *Trans. Nonferrous Met. Soc. China* 24 (2014) 3152–3157
- [47] X.X. Zhang, M.F. Qian, Z. Zhe, L.S. Wei, G. Lin, J.F. Sun, Magnetostructural coupling and magnetocaloric effect in Ni-Mn-Ga-Cu microwires, *Appl. Phys. Lett.* 108 (2016), 052401.
- [48] Y.F. Liu, X.X. Zhang, D.W. Xing, H.X. Shen, D.M. Chen, J.S. Liu, J.F. Sun, Magnetocaloric effect (MCE) in melt-extracted Ni-Mn-Ga-Fe Heusler microwires, *J. Alloys Comp.* 616 (2014) 184–188.
- [49] Z. Chen, D.Y. Cong, X.M. Sun, Y. Zhang, H.L. Yan, S.H. Li, R.G. Li, Z.H. Nie, Y. Ren, Y.D. Wang, Magnetic field-induced magnetostructural transition and huge tensile superelasticity in an oligocrystalline Ni-Cu-Co-Mn-In microwire, *IUCrJ* 6 (2019) 843–853.
- [50] W.J. Feng, Q. Zhang, L.Q. Zhang, B. Li, J. Du, Y.F. Deng, Z.D. Zhang, Large reversible high-temperature magnetocaloric effect in $\text{Ni}_{(50-x)}\text{Mn}_{(38+x)}\text{Sb}_{(12)}$ alloys, *Solid. State. Commun.* 150 (2010) 949–952.
- [51] R.C. Zhang, M.F. Qian, X.X. Zhang, F.X. Qin, L.S. Wei, D.W. Xing, X.P. Cui, J.F. Sun, L. Geng, H.X. Peng, Magnetocaloric effect with low magnetic hysteresis loss in ferromagnetic Ni-Mn-Sb-Si alloys, *J. Magn. Mater.* 428 (2017) 464–468.
- [52] F. Chen, J.L.S. Llamazares, C.F. Sánchez-Valdés, F.H. Chen, Y.X. Tong, L. Li, Ni-Co- Mn-Sn quaternary alloys: Magnetic hysteresis loss reduction and ductility enhancement by iron alloying, *J. Magn. Mater.* 485 (2019) 351–357.
- [53] P.O. Castillo-Villa, L. Mañosa, A. Planes, D.E. Soto-Parra, J.L. Sanchez-Llamazares, H. Flores-Zuneiga, C. Frontera, Elastocaloric and magnetocaloric effects in Ni-Mn- Sn(Cu) shape-memory alloy, *J. Appl. Phys.* 113 (2013), 053506.
- [54] S. Fabbri, J. Kamarad, Z. Arnold, F. Casoli, A. Paoluzi, F. Bolzoni, R. Cabassi, M. Solzi, G. Porcari, C. Pernechele, F. Albertini, From direct to inverse giant magnetocaloric effect in Co-doped NiMnGa multifunctional alloys, *Acta Mater.* 59 (2011) 412–419.
- [55] Z.B. Li, S.Y. Dong, Z.Z. Li, B. Yang, F. Liu, C.F. Sanchez-Valdes, J.L. Sanchez Llamazares, Y.D. Zhang, C. Esling, X. Zhao, L. Zuo, Giant low-field magnetocaloric effect in Si alloyed Ni-Co-Mn-In alloys, *Scr. Mater.* 159 (2019) 113–118.
- [56] A. Shen, W. Sun, D. Zhao, J. Liu, Influence of Cr on microstructure and elastocaloric effect in Ni-Mn-In-Co-Cr polycrystalline alloys, *Phys. Lett. A* 382 (2018) 2876–2879.
- [57] F. Xiao, M.J. Jin, J. Liu, X.J. Jin, Elastocaloric effect in $\text{Ni}_{50}\text{Fe}_{19}\text{Ga}_{27}\text{Co}_4$ single crystals, *Acta Mater.* 96

(2015) 292–300.